Chapter 4

Emergence of Metamagnetic transition, Re-entrant cluster glass and Spin Phonon Coupling in Tb_2CoMnO_6

4.1. Introduction:

The DP (having $A_2BB'O_6$ formula) materials have drawn invigorated research attention due to the existence of magnetic and electric order owing to their potential for practical application in spintronic devices [152]–[156]. Particularly, the DPs having B=Co, Ni, and B'= Mn, are promising candidates for the spintronic applications. These DPs show a low symmetry structure from orthorhombic to monoclinic ($P2_1/n$) and thus the properties of the DPs system depend upon the fully or partially ordering of B/B' ions[159]. The ordered DPs exhibit ferromagnetism which can be unravelled by the Goodenough-Kanamori rule as a result of the 180^0 positive super-exchange interactions between B=Co^{2+}/Ni^{2+} and B′=Mn [16], [88]. However, during the sample preparation, some unavoidable Co^{3+}/Ni^{3+}/Mn^{3+} ions arise in the system which induces ASD in the system [17], [121], [159]. As a result of super-exchange interactions Co^{3+}—O^{2-}—Mn^{3+}, Co^{3+}—O^{2-}—Co^{3+}, Mn^{3+}—O^{2-}—Mn^{3+}, Mn^{4+}—O^{2-}—Mn^{4}, Co^{2+}—O^{2-}—Co^{2+} generates additional AFM interactions in the system [9], [105], [162]. A competition between the FM and AFM interactions commences raising the spin frustration in the system which on reaching a critical level leaves the system in a randomly frozen state, on lowering the temperature, known as the SG state [9], [101]–[105]. The SG states observed in such DPs are the manifestation of the nano-scale inhomogeneity which is the subject of prime interest in solid state research in recent times owing to its complexity and interesting aspects viz., memory and aging effects, slow relaxation, thermo-magnetic irreversibility, etc [71], [103], [104], [112], [191]–[194].

Furthermore, recently, some interesting properties such as; large rotational magnetocaloric effect (MCE), and relaxor glass transition in TCMO have been reported [36-39]. In addition, in our previous work, we have also established that TCMO has a complex spin dynamic which triggered some interesting phases. Hence, an intricate investigation of TCMO may disclose appealing magnetic, structural, and electronic properties. Moreover,

the ionic radius of A site rare earth element plays an important role in SPC in the system which may lead to the induction of ferroelectricity in the system [123], [195]–[197]. Earlier Kumar et al. studied the effect of the ionic radius of A site rare earth and showed changing the A site from La to Nd weakened the SPC [196]. Moreover, theoretical prediction on Y_2NiMnO_6 also established the role of the A site in DP systems [115]. A smaller ionic radius at A site makes large octahedral distortion which extensively plays a vital role in the coupling between degrees of freedom to magnetic ordering. Thus, in the present work, we have shown the role of the lower ionic radius (at A site) of DP systems in the SPC by investigating the Raman effect and magnetic properties in detail. Moreover, we have also investigated the XAS, XMCD, and DFT calculation which is well correlated with the magnetic properties.

4.2. Experimental Details:

TCMO polycrystalline sample was synthesized by conventional solid-state reaction using high purity Tb_4O_7, CoO, and Mn_2O_3 (99.99%) oxide powders as discussed in the previous chapter. The XAS and XMCD measurements of Co-$L_{2,3}$ and Mn -$L_{2,3}$edges were carried out at BL-14 beamline with polarized X-ray at Hiroshima Synchrotron Radiation Centre (HiSOR) [198]. In our case, the TEY mode has been used for recording XAS spectra. The neutron diffraction measurement was performed by neutron powder diffractometer (λ=1.2443 Å) at the Dhruva reactor in Bhaba Atomic Research Centre, Mumbai, India. The magnetization measurement was performed by the SQUID-VSM which is based on the Quantum design-MPMS. The room temperature Raman spectra were performed by Renishaw Via Raman spectrometer with solid state laser delivering the power of 5 mW mm^{-2} and the wavelength of 532 nm line of a diode-pumped by the slow scan rate. The temperature-dependent Raman measurement of TCMO was carried out with LABRAM-

HR800 using the He-Ne laser of the wavelength of 632.8 nm within the temperature range of 10-300 K in the UGC-DAE Consortium for Scientific Research, Indore, India.

4.3. Result and discussion:

4.3.1. Theoretical study:

We have carried out the ab initio calculations based on DFT using the Vienna *ab* initio simulation package (VASP) in the theoretical study [76]. The exchange-correlation potential (Perdew-Burke-Ernzerh of exchange-correlation functional) is treated within the generalized gradient approximation (GGA) [199]. The projector augmented wave method (PAW) is adapted to describe the core-valence interaction [200]. The calculations were executed with 6×5×4 K-mesh. We have considered the on-site coulomb correction (GGA+U) for calculating the spin-polarized partial and total DOS. The typical choices of Hubbard U corrections are applied to be ~3 eV for Tb-4f states, ~4 eV for Co-3d states and ~3 eV for Mn-3d states [201], [202]. Calculations were performed both for FM and AFM couplings among spins. However, the calculation predicts an FM ground state of TCMO as the FM interactions are obtained as energetically favorable. The total density of states (TDOS) of TCMO for the FM interactions is carefully observed (Fig. 4.1). An insulating nature of the system is indicated by the absence of any states near the Fermi level. Moreover, the dominant contribution is coming out from Tb-*f,* Co-*d,* Mn-*d* and O-*p* states with their respective spin integrated projected density of states (PDOS). The notable hybridization among Co/Mn-*3d* and O-*2p* states is clearly shown in the PDOS curves. The large asymmetry is observed in Co-*3d* and Mn-*3d* PDOS which clearly suggests the FM nature of both ions (inset of Fig. 4.1). The corresponding magnetic moment of Co and Mn is found to be ~2.6μ_B and ~1.53μ_B, respectively. However, O-*2p* PDOSs are not showing any considerable spin polarization (asymmetry) and hence indicating the non-magnetic nature of this.

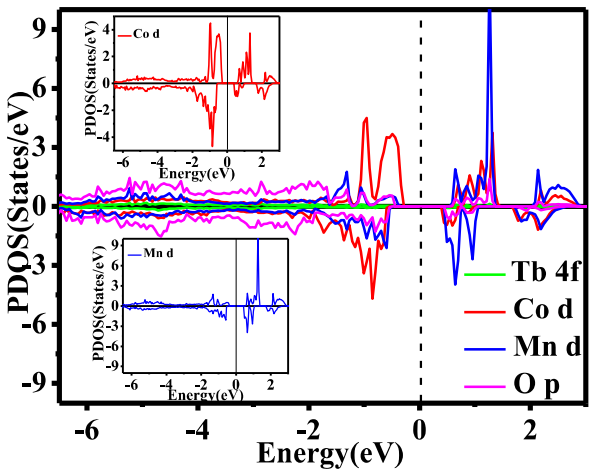

Fig. 4.1 Spin resolved PDOS for Tb-4f, Co-3d, Mn-3d, and O-2p orbitals. Top and bottom insets: the PDOS (enlarged) of Co-3d and Mn-3d PDOS of TCMO, respectively.

4.3.2. X-ray absorption and X-ray magnetic circular dichroism study:

Fig. 4.2(a) depicts the XAS spectra of the Mn-$L_{2,3}$ edge which exhibits broadly two spin-orbit splitting peaks of Mn $L_3(2p_{3/2})$-edge and Mn $L_2(2p_{1/2})$-edge at 82 K. These two peaks arise due to the dipole transition from 2p core level to 3d unoccupied levels. XAS spectrum of L_3 edge shows two clear peaks in which lower energy peak is the signature of Mn^{3+} state whereas higher energy peak is associated to Mn^{4+} state (Fig. 4.2(a)). Similarly, the L_2 edge is also suggesting the signature of Mn^{3+} and Mn^{4+} valance states in TCMO [173], [203].

In Fig. 4.2(b) the XMCD spectra of the Mn-$L_{2,3}$ edge is also showing the clear signature of the mixed oxidation states of Mn ion (Mn^{3+} and Mn^{4+}). The spectra depict a considerable XMCD signal which indicates the presence of magnetic nature of Mn cation at 82 K. Moreover, Mn L_3-edge resides opposite the Mn L_2-edge which suggests spin moment is significantly involved in magnetic properties. Oppositely directed peaks in the XMCD signal clearly indicate the effective FM nature of the Mn cations [173], [204]. The XAS spectrum at room temperature has been shown in the inset of Fig. 4.2(b). No significant XMCD signal is observed indicating the absence of any magnetic ordering at room

temperature (not shown here). However, the XAS spectra at 300 K also indicate the presence of mixed-valence states of Mn cation.

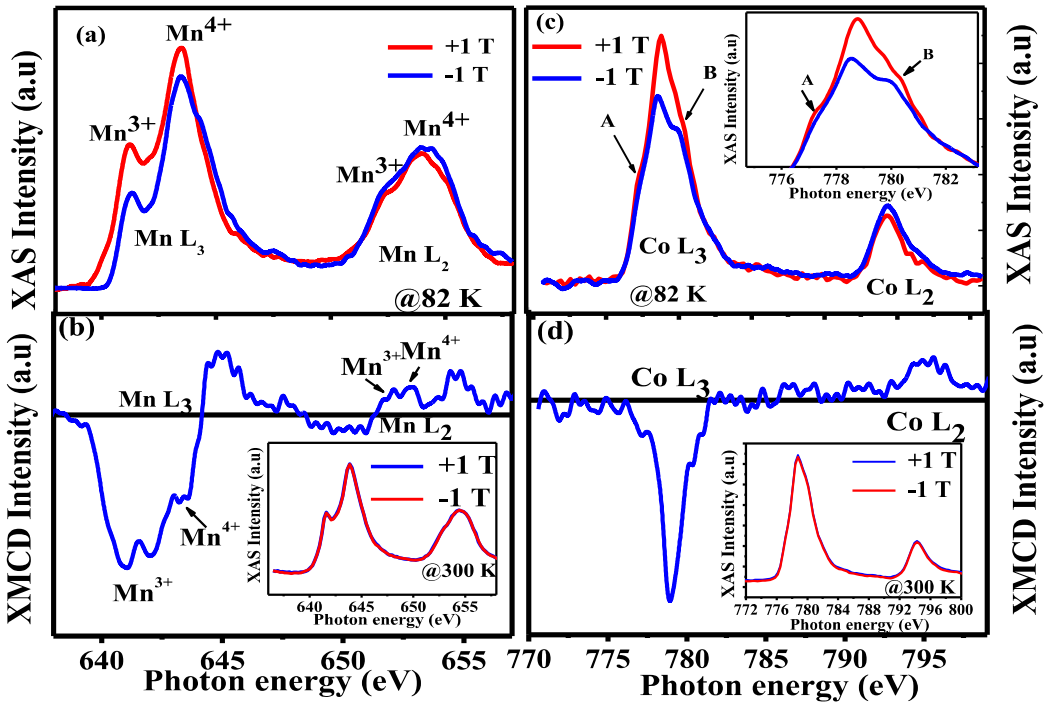

Fig. 4.2: (a) XAS spectrum and (b) shows the XMCD spectrum of Mn $L_{2,3}$ edge at 82 K. The inset of (b) XAS spectrum of Mn $L_{2,3}$ edge at 300 K. (c) the XAS spectrum and (b) XMCD spectrum of Co $L_{2,3}$ edge at 82 K. Inset of (c): the close look of lower energy shoulder of Co $L_{2,3}$ edge. And the inset of (d) XAS spectrum of Co $L_{2,3}$ edge at 300 K.

Fig. 4.2(c) demonstrates the XAS spectra of Co-$L_{2,3}$ edge at 82 K. The spectrum is ascribed to the transition of electrons from Co 2p core level to Co 3d unoccupied level which is directly related to the valence state and very sensitive to the spin state of Co cations. The spectrum is mainly composed of two spin-orbit splitting peaks which are associated with Co $2p_{3/2}$ (at 778.8 eV) and Co $2p_{1/2}$ (at 794 eV). For the Co^{2+} oxidation state, the main peak lies at around 779 eV, and a pronounced shoulder (named as A) for Co^{2+} in the HS state at 777 eV [205], [206]. Whereas for the $EuCoO_3$, Co L_3 XAS spectra show a shoulder-like feature (named B) at relatively higher energy in which Co^{3+} ions are in an LS state [86].

Thus, for the system under investigation, the position of the L_3 edge peak and a close look at the shoulder at 777 eV (inset of Fig. 4.2(c)) describes the presence of HS state of Co^{2+} and higher energy shoulder confirms the presence of Co^{3+} in LS state. Additionally, looking into the L_2 edge of Co XAS spectra relatively sharp and narrow peak is also suggesting the presence of Co^{3+} cation in the LS state. Thus, the above features suggest the presence of a mixed oxidation state of Co cation in the TCMO. The corresponding XMCD signal of the Co-$L_{2,3}$ edge at 82 K is shown in Fig. 4.2(d). The XMCD signal of both the edges L_2 and L_3 confirms the involvement of spin moment of Co ion. As Co^{3+} is possibly in the LS state, its spin moment is zero and will not participate in the total spin moment of system. No measurable XMCD signal was detected at room temperature, suggesting the lack of magnetic ordering at room temperature (not shown here). The XMCD spectra of Mn- and Co-edges at 82 K suggest FM behavior of the system which is absent at room temperature.

4.3.3. Magnetic Study:

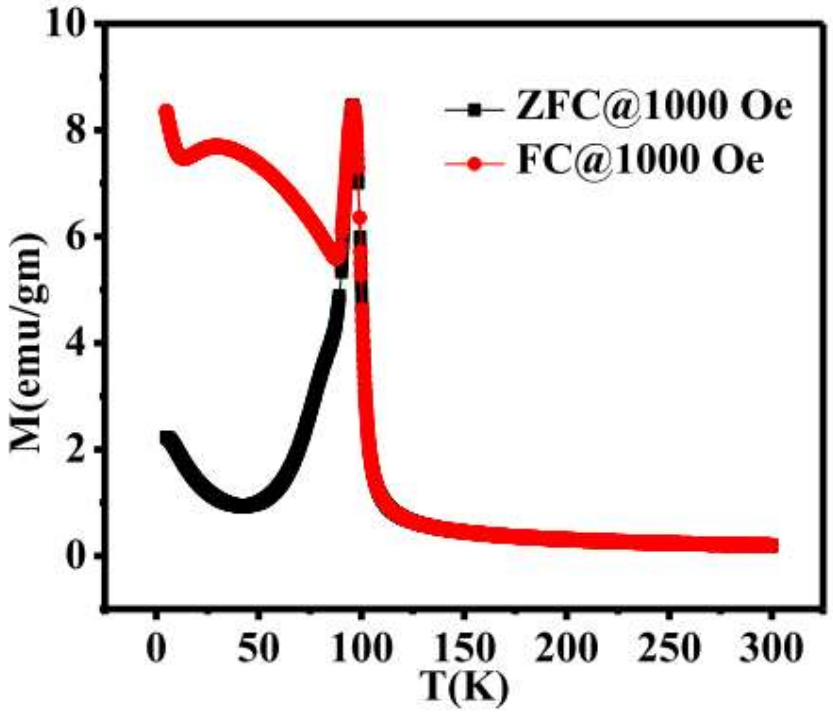

Fig. 4.3: The ZFC-FC curve at the applied dc field of 1000 Oe of TCMO.

The conventional ZFC and FC magnetization (M) with the applied dc field of 1000 Oe in the temperature range 2-300 K has been illustrated in Fig. 4.3. The abrupt change in the M(T) curve for both the modes at 100 K is clearly suggesting the FM transition. The previous chapter on the TCMO system also confirmed the LRO at 100 K (Fig. 3.5) [207]. Moreover, the large bifurcation indicates frustration in the system [178], [208]. Apart from this, the presence of frustration due to the ASD and mixed valence state is also suggested by the observation of the reduced saturation magnetization (M_s) at 5 K as displayed in Fig. 4.4(b). The M_s is estimated by the linear extrapolation method which comes out to be 14.98μ_B/f.u. On the other hand, the theoretical saturated magnetic moment can be calculated by the formula [2gJ +6]μ_B, where 6μ_B is arising from the FM alignment of the Co/Mn sublattice and gJ is related to the rare earth moment [11], [209]. The value of the theoretical moment is calculated to be 24μ_B/f.u which is larger than that obtained experimentally. This deviation might be due to the presence of partial AFM alignment of Co/Mn moments (due to the presence of the ASD and Co^{3+}/Mn^{3+} ions) and canting of rare earth elements at low temperatures. Hence, the antiphase boundaries (APBs) originated by the inherent ASD of the system can also contribute to the reduction of the observed moment in addition to the compensation of magnetic moment as required by the magnetic structure. Fig. 4.4 illustrates the M(H) loops at different temperatures. The M(H) curves observed at relatively higher temperatures (25 K and 50 K) show characteristically different behavior than those observed at lower temperatures (T= 2 K & 5 K). However, the hysteresis curves observed at 2 K and 5 K show almost similar patterns while the only noticeable difference that can be observed is slightly lower magnetization for the lower temperature M(H) curve (inset of Fig. 4.4(a)). This result may be associated with the well-established antiparallel alignment of PM Tb^{3+} spins by the internal field of the FM Co/Mn sublattice at low temperatures [10]. Our M(T) (ZFC curve) also supports this by showing an anomaly below

7 K. Another possible reason for smaller magnetization at low temperature (below 5 K) might be due to the canting of spin. As the temperature decreases, the canting between the spin increases and gives rise to the lower value of magnetization [105]. However, the hysteresis curves at both temperatures are not showing saturation up to the maximum applied field of 5 T. As already stated, ASD leads to different AFM couplings which give rise to such unsaturated M(H) loops. However, the large hysteresis is indicating the predominant FM interactions present in the system. Thus, there is a significant competition between FM and AFM interactions in the present system.

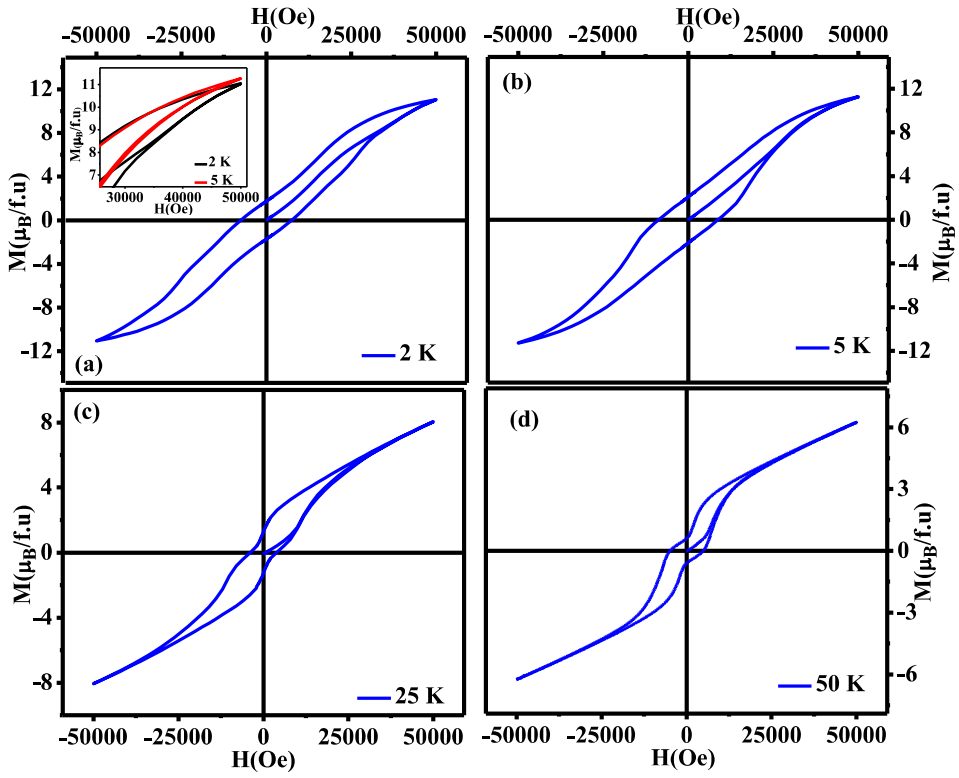

Fig. 4.4:(a), (b), (c) and (d) M(H) curves at 2 K 5 K, 25 K, and 50 K, respectively.

On the other hand, the M(H) loop recorded at 50 K showed a sudden slope change after reaching a certain critical field forming a step-like behavior which is a feature of the

metamagnetic transition (Fig. 4.4(d)). This metamagnetic feature is less prominent at 25 K and disappears on further lowering the temperature (Fig. 4.4(c)). It is relevant to mention here that meta-magnetic steps have been previously observed in DP compounds Y_2CoMnO_6, Eu_2CoMnO_6, and Lu_2CoMnO_6 where the A site is occupied by the non-magnetic ions [8], [210], [211]. The plausible origin of the observation of such meta-magnetic steps may be related to the ASDs which may occur as a point defect or in the group to form APBs producing planar defects. In Co/Mn-based DP systems, the existence of the APBs is commonly observed, and strongly pinned magnetic domain walls are generated by the interaction between the magnetic ions at the APB-domain borders [8]. The possible underlying mechanism for the APB formation in the present system could be such that they are produced by the same number of regions that are enriched in Co^{2+} or Mn^{4+} ions. Due to the existence of the strong AFM interactions across the APBs via Co^{2+}—O^{2-}—Co^{2+}/ Mn^{4+}—O^{2-}—Mn^{4+}, the neighboring FM domains (formed due to the Co^{2+}—O^{2-}—Mn^{4+} super-exchange interactions) are forced to align anti-parallel to each other. Consequently, the saturation magnetization of the M(H) loops gets diminished as well as the strong anisotropic pinning forces across the APBs of the anti-parallel FM domains offer a strong hindrance to the applied magnetic field to orient them along the field direction. Thus, on reaching a critical value of the magnetic field, a sudden rise in the magnetization in the form of the steps is observed. Different sizes and nature of APBs result in the occurrence of steps at the different fields in the M(H) loop. In contrast to the Y_2CoMnO_6 and Lu_2CoMnO_6 systems which are reported to show pronounced steps in their M(H) loops down to the lowest temperatures (2 K) [8], [210], the present system TCMO exhibited meta-magnetic steps only at higher temperatures and on lowering the temperature, the steps disappeared. This is might be associated with the 3*d*-4*f* interactions owing to the magnetic nature of the Tb ions. However, the ordering of Tb starts below 9 K hence there might be

another plausible reason related to the blocked regime which generates due to the coexistence of two phases through different interactions [212]. These competitions between interactions eventually lead to frustration or glassy features in the system. TCMO enters into the glassy phase below T_G~33 K (discussed below in detail), and metamagnetic steps decrease (at 25 K) below T_G and most prominent (50 K) above this. Thus, it is seemingly associated with the SG state present in the system. However, the observation of an anomaly around 40 K in the M(T) curves may indicate the emergence of a secondary phase near this temperature (Fig. 4.3(a)). Unlike the dc susceptibility measurements, ac susceptibility measurement is a magnificent tool to probe into the spin dynamics and hence to investigate glassy behavior [101]. We have studied the ac susceptibility at a lower temperature range (<60 K). Fig. 4.5(a) shows the temperature variation of χ_{ac}''. The clear peaks in χ_{ac}''(T) are observed at ~ 33 K. The observed broad and clear frequency-dependent χ_{ac}''(T) peaks are suggesting that the system enters into a glassy state. Such peaks are the manifestation of the underlying slow spin relaxations in the glassy state [18], [101], [104]. The observation of such low-temperature glassy peaks despite having a higher temperature LRO is a typical feature of the RSG state.

We have fitted the data with different models for getting further insights into the RSG state. We have calculated the Mydosh parameter (p) from the frequency dependence of the ac peaks which is known as a universal tool to probe the SG state [101]. Here,

$$\boldsymbol{p} = \frac{\Delta \boldsymbol{T_f}}{\boldsymbol{T_f \Delta log_{10}(f)}}, \qquad 4.1$$

Where $\Delta T_f = T_{f1} - T_{f2}$ and $\Delta log_{10}(f)$=$log_{10}(f1)$-$log_{10}(f2)$. P lies between 0.005 and 0.08 for typical SG or CG systems, while for the superPM system, the p-value is larger than 0.2. The value of p comes out to be ~ 0.07 for TCMO confirming the glass type state.

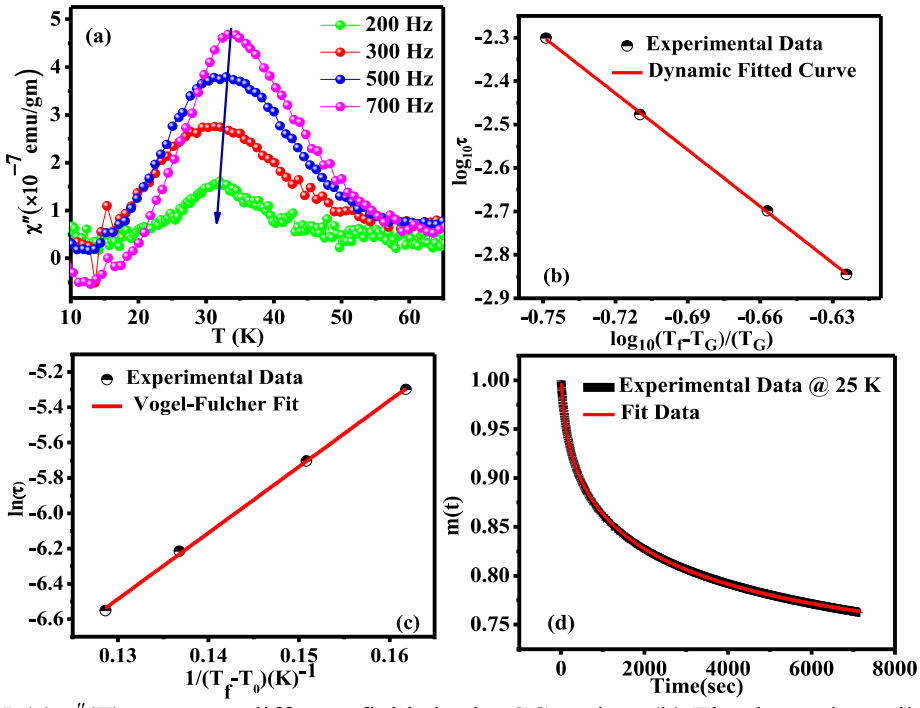

Fig. 4.5:(a) χ''(T) curves at different fields in the CG region. (b) The dynamic scaling fit to the log-log plot of "τ(=1/f) vs. $(T_f-T_G)/T_G$)" and (c) the V-F fit to the log-log plot of "τ vs. $1/(T_f-T_0)$". (d) KWW fit to the m(t) data recorded at 25 K.

Moreover, below the critical temperatures T_f. the spin dynamics get slowed down in an SG or CG state. We can explore the critical slowing down of spins near T_f by using the dynamic scaling law [18], [104]

$$\tau = \tau_0 \left(\frac{T_f - T_G}{T_G}\right)^{-z\nu} \qquad 4.2$$

Where f is the excitation frequency associated with the characteristic spin-flip time ($f_0=\frac{1}{\tau_0}$); T_G is the equivalent SG freezing temperature which is within the limit of $f \to 0\ Hz$ and $H_{DC} \to 0\ Oe$, and f_0 is the characteristic spin flipping time (τ_0) as $f_0=\frac{1}{\tau_0}$; zν is known as the dynamical critical exponent. "$\log_{10}(\tau)$ vs. $\log_{10}(\frac{T_f-T_G}{T_G})$" curve has been plotted in Fig. 4.5(b). The obtained value for the best fitting with the above dynamical scaling law comes out to be: f_0~3.5×10^5 Hz ($\tau_0 = 2.82\times10^{-6}$ s), T_G = 27 K, and the exponent zν is found to be ~ 4.4 which is satisfied for the SG state (4<zν< 12). The obtained value of τ_0~10^{-6} s is

greater by a few orders from the value for a canonical SG system that typically lies between ~10^{-12}-10^{-13} s. The larger spin flipping time is indicating that the observed transition is because of the freezing of finite-sized clusters (which take more time to relax) rather than individual spins [18], [103], [104].

The empirical Vogel-Fulcher (VF) law can also be employed to fit the curve "*f* vs. T_f", for further probing of inter-cluster interactions. The law being of the form [104], [213]

$$\tau = \tau_0 \exp\left(-\frac{E_A}{K_B(T_f - T_0)}\right); \quad 4.3$$

Where T_0 is formally known as the VF parameter which represented the strength of inter-cluster interaction in the form of temperature. f_0 is known as a characteristic spin-flip time, and E_A is the activation energy. Fig. 4.5(c) shows the linear fitted graph "ln(τ) vs. $1/(T_f - T_0)$'' using the V-F law. The best fitting gives $\tau_0 \sim 10^{-6}$ Hz (the yielded value of τ_0 is of the same order as the previous dynamic scale fitting), T_0=25.55 K and E_A/K_B=37.47 K. The comparable values of T_0 and activation energy suggest the existence of intermediate inter-cluster couplings in the TCMO as the larger value of activation energy than T_0 denotes weak coupling and the smaller one indicates strong coupling [214]. The presence of interacting magnetic spin clusters is again indicated by the yielded large value of $\tau_0 = \frac{1}{f_0}$.

Another experimental tool to realize the slow spin relaxation can be found in the "time (t) evolution of remanent magnetization m(t)" in the SG or CG state below T_f. The measurement was performed according to the FC protocol. First, the TCMO system was cooled down to 25 K (below T_f) with a field H=0.1 T and after switching off the magnetic field the TRM data was recorded. Fig. 4.5(d) illustrates the normalized magnetization $m(t)=\left(\frac{M_t}{M_{t=0}}\right)$ as a function of time. The TRM data can be fitted by the KWW stretched exponential equation as shown below [71], [192]:

$$m(t) = m_0 - m_g exp\left\{-\left(\frac{t}{\tau}\right)^{\beta}\right\}; \quad 4.4$$

Here, m_g is associated with the magnetization of glassy components, m_0 represents the initial remanent magnetization, τ is the characteristic relaxation time constant, and β is known as the stretching exponent or the shape parameter. For the analysis of TRM data, another power law has also been often used as m(t) $\propto t^{\pm\alpha}$[72]. As a matter of fact, we tried to fit our TRM data with both the above relations but the best fitting is found for the KWW model which is shown in Fig. 4.5(d). The fitting with the power law ($t^{\pm\alpha}$) comes out to be unsatisfactory (not shown here). For disordered or glassy systems, the KWW fitting is a powerful tool and it is widely used for the analysis of the m(t) data [192]. The value β lies between 0 and 1, for the different class of disordered systems. Thus, for the TCMO system, the existence of a glassy state has been confirmed as the obtained value of β (~0.44), at this temperature (25 K). Therefore, all the above facts verified that the system is entering in the RCG state at low temperatures. However, the co-existence of low-temperature glassy state and the high-temperature LRO have been reported in the systems such as DP, disordered ferromagnet La_2NiMnO_6, $La_{1.5}Sr_{0.5}CoMnO_6$, spiral magnet $BiMnFe_2O_6$, and antiferromagnet Pr_2CoFeO_6 etc[9], [18], [71], [105]. Present system TCMO contains the major microscopic ingredient for glassy transitions is B-site disorder [9], [18], [105], [106], [162]. The domain formation involves microscopic time scales in pure FM or AFM systems but because of the presence of disorder, it attributes pinning of the domain wall which essentially causes metastable states [106], [215]. Thus, in the experimental time scale, the system cannot achieve an equilibrium state which eventually caused a non-equilibrium phase like spin-relaxations, aging effects, etc [106], [215]. However, the frustration might be due to the random magnetic anisotropy in the TCMO system. Magnetic anisotropy creates an easy and hard axis which introduces interdependence on the direction of spontaneous magnetization and the internal energy of the system and thus induces frustration in the present system [216]. Moreover, Bedanta, et. al stated that the lattice that

crystalline in a low symmetry structure produces larger magnetic anisotropy energy (as TCMO is crystalline in space group $P2_1/n$ (14)) which again supports the presence of larger anisotropy energy in this system [216]. Interestingly, our earlier work on TCMO describes the presence of large anisotropy energy [207]. Hence, the magnetic anisotropy energy may play a significant role in inducing the (CG) phase in the present TCMO system.

4.3.4. Temperature-dependent Raman study:

Raman scattering is a very useful technique to probe into the lattice distortion in the system while the temperature-dependent Raman scattering can be used to investigate the SPC in the system. The substitution of smaller rare earth element Tb at the A site can result in structural distortion and can be coupled with the spin states in TCMO. All the atoms are Centro symmetrically situated in the ideal perovskites with the structure $Pm\bar{3}m$ hence these systems do not show any Raman mode. However, the B/B'O_6 octahedral distortion or shifts in R results in the removal of the degeneracy of Raman modes. Moreover, some r-points also become Raman active [217]. For the disordered DP, orthorhombic structures (Pbnm space group) where B and B' cations are randomly distributed show less number of modes (which is similar to ABO_3 systems) [121], [218]. On the contrary, additional Raman modes are visible in the monoclinic symmetry[196], [219]. 24 Raman active optical modes are predicted by the lattice dynamic calculations in which the irreducible representation of the 2/m factor point group is $12A_g+12B_g$. In which internal modes due to the oxygen octahedral reside above 380 cm^{-1} and the lattice modes are observed below 380 cm^{-1} [195], [220]. The Raman spectra at 300 K have been shown in Fig. 4.6(a). The Raman spectrum at room temperature has been decomposed by the number of Lorentzian functions and its enlarged view has been illustrated in the inset of Fig. 4.6(a). 7 Raman active modes have been observed out of 24 and the most intense peak has been observed at 630 cm^{-1}. The most intense Raman mode at 630 cm^{-1} is associated with the stretching vibration of Mn/CoO_6

octahedral. Similarly the modes at 630 cm^{-1}, 500 cm^{-1}, 466 cm^{-1}, 334 cm^{-1} and 293 cm^{-1} may be assigned to A_g symmetry whereas the modes at 535 cm^{-1} and 399 cm^{-1} have B_g symmetry [196], [219]. In TCMO, less number of Raman modes are visible at room temperature than in YCMO, which can be understood by the lower ionic radius of Y [219]. Similarly, in TCMO, a large number of modes are visible than in La-based DP [17]. The refinement of the NPD and XRD pattern of TCMO is successfully fitted by the $P2_1/n$ space group at 300 K which is well consistent with the Raman spectra at room temperature.

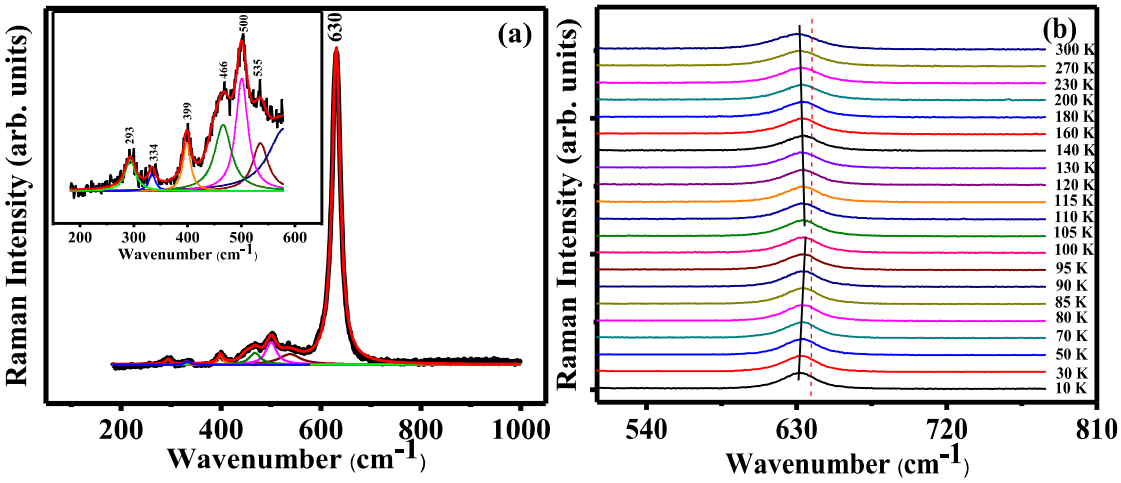

Fig. 4.6: (a) The Raman spectra at room temperature fitted by the number of Lorentzian functions and its inset: the enlarged view of fitted peaks below Ag mode. (b) Raman spectra at different temperatures.

Fig. 4.6(b) shows the variation with temperature from 10 K to 300 K of the Raman spectra (scattering intensity with Raman shift) of TCMO. No remarkable shape change suggests the absence of any phase change in the system. As discussed above TCMO has the onset of magnetic ordering (PM to FM phase) below 100 K. Fig. 4.6(b) shows the effect of the magnetic ordering on the lattice vibrations in the system. To further investigate the SPC of the present system, we analyzed the impact of temperature on the phonon behaviour of the

behavior of the most intense mode (stretching mode at 630 cm^{-1}). Fig. 4.7(a) illustrates the temperature variation with the Raman excitation frequency of the stretching mode. Balkanshi has proposed that the behavior of phonon is mainly contributed by the anharmonicity (due to the usual lattice contraction), in the absence of any phase transition [221]. In this model, the phonon excitation wavenumber is described by the following expression

$$\omega_{anh} = \omega_0 - C\left(1 + \frac{2}{e^{\frac{\hbar\omega_0}{K_B T}}}\right) \quad 4.5$$

Where C and ω_0 are the adjustable parameters, $\hbar$ is reduced Planck's constant, T is the temperature and K_B is Boltzmann's constant. According to this model, due to an anharmonic effect, usually, the phonon modes get hardened and at sufficiently low temperature attain the plateau-like region, with cooling the sample [123], [222]. This behavior is generally obtained in the absence of SPC. Fig. 4.7(a) clearly indicates that the stretching mode gets hardened and follows the anharmonic behavior (orange line) down to the transition temperature (Tc). This indicates that the anharmonic effect is a dominant contribution to the temperature dependence of stretching mode down to Tc. Below Tc, the phonon frequency has deviated from the anharmonic behavior. Thus, the observation of anomalous softening in the phonon mode near Tc illustrates the involvement of vibrations of magnetic ion which affects the modulation of lattice vibration and results in SPC.

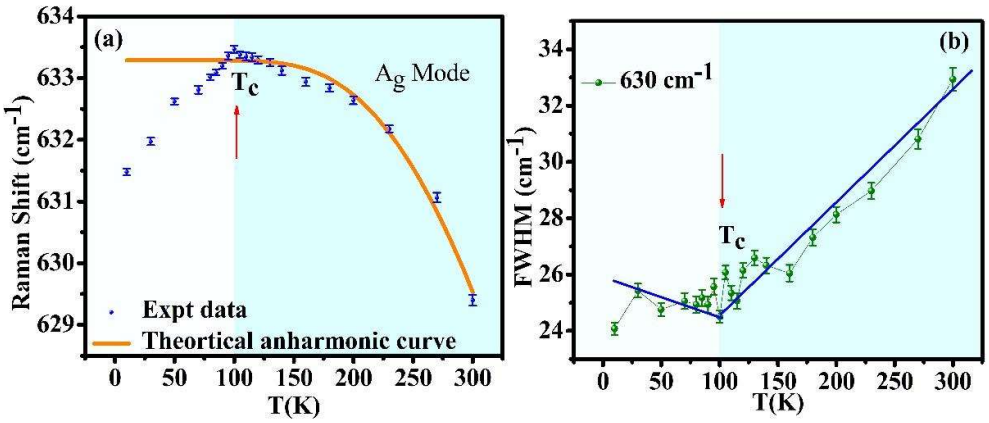

Fig. 4.7:(a) The anharmonic fit to the temperature-dependent Raman shift of stretching mode. (b)Temperature variation of the FWHM of the stretching mode.

It is relatable to discuss the effect of magnetostriction (change in lattice constant and cell volume) on the observed phonon anomaly as the full-width half maxima (FWHM) is influenced differently by magnetostriction and SPC. This, earlier Rosivaldo X. Silva et. al. discussed that in YCMO, the anomaly in phonon modes near transition temperature is the result of the magnetostriction effect [219]. To understand the origin of the earlier discussed phonon anomaly we have plotted the FWHM of the stretching mode with temperature (Fig. 4.7(b)). The linewidth of the phonon modes is related to the lifetime of the phonons. It is determined by the dominating scattering mechanism which could be temperature-dependent scattering from the phonons and temperature independent from the lattice defects [223]. It suggests that the FWHM or linewidth of the phonon remains unchanged by subtle changes that occurred in lattice parameters due to magnetostriction effects. On the other hand, it is influenced by the magnetic transition by showing the anomaly in FWHM near the magnetic transition [223], [224]. The FWHM shows the change in slope across the magnetic transition (Fig. 4.7(b)). The FWHM broadening (or the decrease in linewidth) clearly indicates the decrease in phonon lifetime beyond T_C. Thus, the phonon is coupled by the magnetically ordered spin below the LRO and creates some additional phonon decay modes. Another possibility that could affect the phonon lifetime is electron-phonon coupling. The earlier research on TCMO and the DFT calculations established the

insulating nature of the system which eliminates the prospecting of electron-phonon coupling [116]. Hence, the observed phonon anomaly in TCMO is solely ascribed to the coupling between spin and phonon.

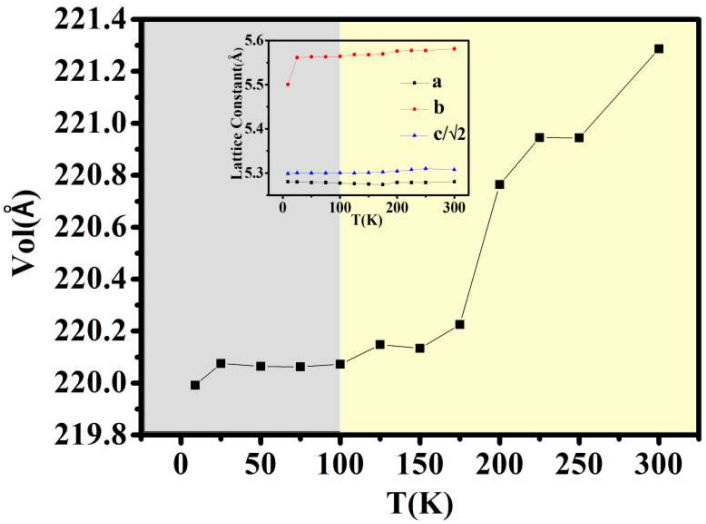

Fig. 4.8: The temperature variation of cell volume while its inset presents the lattice parameters at different temperatures extracted from NPD measurement.

To further eliminate the effect of magnetostriction in the obtained phonon anomaly, we can employ the lattice parameters obtained from the temperature-dependent NPD measurements. The magnetostriction effects can be directly illustrated by prominent changes in the lattice parameters or the volume of the unit cell across Tc [223], [225]. The temperature variation of the lattice parameter of the unit cell and the volume of the unit cell acquired by the Reitveld refinement of the NPD pattern is shown in Fig. 4.8. The lattice parameters/cell volume curves are not showing any remarkable anomaly across the Tc which clearly reveals the absence of magnetostriction effect in the present system. Therefore, the above facts univocally ascribed that the phonon anomaly of the present system is entirely associated with the entanglement between spin and phonon which cause the SPC.

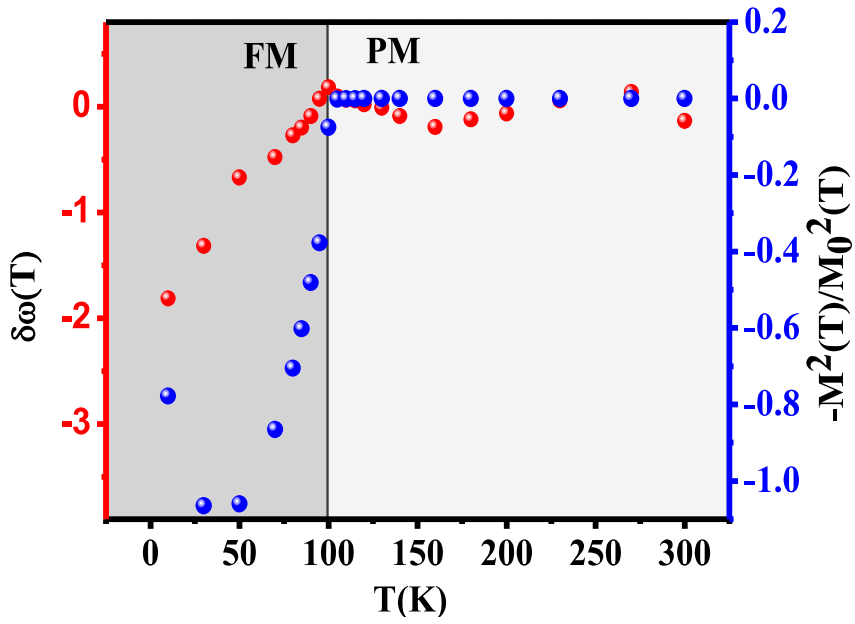

Fig. 4.9: Thermal variation of δω(T) and $\left(\frac{M(T)}{M_0}\right)^2$ of A_g stretching mode.

Furthermore, to establish the origin of the softening of phonon mode, we have plotted the renormalization of phonon frequency with normalized magnetic moment (Fig. 4.9). According to the mean-field theory, the LRO induced the renormalization of phonon frequency which is proportional to spin-spin correlation function ($<S_iS_j>$) of the nearest neighbor spins localized at the i^{th} and j^{th} sites [97], [218]–[220]. The frequency difference between the observed and the calculated phonon modes by the anharmonic model should follow the same trend as the normalized magnetic moment obtained from the magnetization data as follows:

$$\delta\omega(T) = \omega(T) - \omega_{anh} \propto \left(\frac{M(T)}{M_0}\right)^2 \quad 4.6$$

Here, M(T) represents the magnetization at temperature T, M_0 represents the maximum magnetization and δω(T) is the frequency difference obtained by calculated and observed phonon modes. Fig. 4.9 shows the good overlap of both the modes down to the Tc and shows downturn behavior at the same temperature (T_c). Therefore, all these facts again

ascertain the presence of a strong interplay between the microscopic degree of freedom via SPC in the system. Hence, the above analysis established the interplay between phonon renormalization and the magnetic spin in the TCMO system.

4.4. Conclusion:

The DFT, Electronic structure analysis by XAS, and magnetic and Raman spectroscopy have been investigated for TCMO polycrystalline DP. The FM transition is observed at ~100 K. However, with decreasing temperature the presence of AFM along with FM state is also observed. The observed metamagnetic step-like behavior in the M(H) curve can be explained by the drastic reorientation of the pinned domain. These domains are aligned antiparallel by the APBs at zero fields. The disorder decreases the magnetic ordering, as well as the homogeneity of APBs, giving rise to sudden slope change in the hysteresis loop. This disorder further leads to spin frustration at low temperatures (~33 K). The obtained larger value of spin-flip time (τ_0) suggests the freezing of the spin cluster instead of a single spin. The anharmonic softening in the stretching Raman mode below T_c and the deviation from the anharmonic behavior reveal the coupling between the phononic degree of freedom and spin in the system. The model obtained by the mean-field theory also confirmed the presence of entanglement between spins and phonon in TCMO. The theoretical calculation is consistent with that of the experimentally observed behavior